Journal of Power Sources, 42 (1993) 119–135

A photocurrent imaging study of the distribution of lead monoxide in corrosion layers on lead/acid battery grids

R. Peat* and P. T. Moseley
AEA Industrial Technology, Harwell Laboratory, Didcot, Oxon OX11 0RA (UK)

A. F. Hollenkamp and D. A. J. Rand
CSIRO, Division of Mineral Products, P.O. Box 124, Port Melbourne, Vic. 3207 (Australia)

Abstract

It is widely believed that α-PbO is a principal contributor to premature capacity loss in lead/acid batteries via the formation of a resistive 'barrier' layer in the corrosion zone of the positive grid. While batteries employing Pb–Ca grids are more prone to capacity loss than those using Pb–Sb grids, a definitive relationship of such behaviour with α-PbO distribution on either of these two alloys has yet to be demonstrated. In the work reported here, *ex situ* scanning laser imaging has been used to reveal the distribution of the α-PbO phase across paste/corrosion layer/grid transverse sections of cycled Pb–Ca grids. The technique has been successfully extended to *in situ* measurements of localized photocurrent at potentials that correspond to the environment of the positive plate in a lead/acid battery. It has been demonstrated that α-PbO films can be mapped at a resolution that provides an intimate insight into their influence on battery operation.

Introduction

Environmental concern over toxic gas emissions from internal combustion engines has encouraged some major American and European cities to introduce government legislation to force the development of zero emission vehicles by the end of the twentieth century. There are several major problems to be overcome if lead/acid batteries are to maintain their present status as the main form of energy storage for electric vehicles: energy density must be raised; power density must be improved towards the end of discharge; cycle life must be extended; charging must be rapid; the battery must be maintenance free. Under duties that demand repeated deep-discharge cycling regimes such as those required for motive-power applications, it is well known that cells with positive plates based on grids of lead, as well as on Pb–Ca, Pb–Ca–Sn and Pb–Sb (<2 wt.% Sb) alloys, all exhibit inferior performance compared with equivalent high-antimony plates (>5 wt.% Sb). When subjected to such service, antimony-free and low-antimony batteries tend to exhibit an early and rapid walkdown in deep-discharge capacity [1–11]. On the other hand, maintenance-free operation under deep-discharge cycling conditions requires the antimony content in the grid alloy to be low due to the adverse effect of this constituent on gassing rates and, hence, water loss. It is this conflict between the virtues of antimony (assists capacity

*Author to whom correspondence should be addressed.

0378-7753/93/$6.00

retention) and the detrimental effects of antimony (increases water consumption) that has prompted a considerable amount of research on what has come to be termed the 'antimony-free effect'. It should be noted, however, that since both antimonial and calcium grids can exhibit this phenomenon, it is more accurate to express the problem as 'premature capacity loss', PCL [12].

In general, explanations of the mechanism of PCL in positive plates fall into two categories. Some workers favour a modification of the active mass, whereas others claim that an insulating barrier is formed between the grid and the active material. The former is embodied in the aggregate-of-spheres model [13] and emphasizes the loss in capacity performance in terms of changes in the conductivity and the connectivity of the constituent particles. The second school of thought asserts that resistive compounds such as α-PbO and $PbSO_4$ are formed preferentially at the grid/active-material interface to give a 'barrier' layer [5, 7, 9, 11, 13–15].

Some studies have shown [3, 5, 9] that the corrosion film formed on battery grids has a duplex structure that comprises a dense inner layer of α-PbO deposited directly on the grid surface beneath a compact, but porous, covering of $PbSO_4$. It is also claimed that α-PbO_2 and basic lead sulfates may be present [16, 17]. The $PbSO_4$ is considered to act as a semipermeable membrane that hinders, or blocks, the migration of HSO_4 and SO_4^{2-} ions from the electrolyte within the pores of the active mass [18]. During charging, the net loss of H^+ ions from the interior of the corrosion layer raises the pH and allows α-PbO to form via consumption of the grid. Towards the top of charge, the $PbSO_4$ membrane is oxidized to α-PbO_2, but the α-PbO film may persist, even under conditions of overcharge [19]. In terms of electrical conductivity, $PbSO_4$ is an insulator whereas α-PbO_2 and β-PbO_2 are degenerate semiconductors [20]. Due to structural defects, α-PbO occurs as a semiconductor. Basic lead sulfates are nonconducting [21]. Attention has focused on $PbSO_4$ and/or α-PbO as the most likely candidate(s) for impeding the electrochemical reactions that normally take place at the electrodes.

It has been noted that corrosion layers are more adherent to the grid when Pb–Sb alloys are used and also that there is a lower incidence of stress cracking [22]. This behaviour has been attributed [23, 24] to the formation of a compound $Pb_2Sb_2O_6$ with a layer-type structure that maintains mechanical integrity by allowing a degree of micro-slippage within the corrosion film. It has also been argued that the development of a barrier layer is inhibited by the presence of soluble antimony compounds [18]. Corrosion is more catastrophic with Pb–Ca systems and extends well into the alloy but, fortuitously, the use of small amounts of tin (either alloyed into the positive grid or applied as a surface coating) is helpful in facilitating recovery from deep discharge. Again, there is a considerable diversity of views concerning the mechanism of the tin action, but the general consensus is that the tin modifies the corrosion products and reduces passivation problems [14, 15, 25].

Despite the wealth of information, a full understanding of PCL remains elusive. More information is required on the composition and properties of the materials present in both the active mass and the barrier layer as they exist during cell operation. Although many studies have indicated that α-PbO plays an important role, exact details of the distribution of this phase have been difficult to obtain by conventional techniques such as microscopy (optical or electron) and X-ray diffraction phase analysis. This is due both to the fine scale at which the α-PbO is present and to the lack of contrast between the various phases present in the corrosion product. As a consequence, much of the evidence for α-PbO has been obtained from the *in situ* techniques of photocurrent spectroscopy [16, 17, 21, 26–29] and, to lesser extent, photoacoustic spectroscopy [30].

These techniques preclude the possibility that α-PbO is an experimental artefact induced, for example, by the action of performing the analysis *ex situ*. The α-PbO is particularly favourable for study since the overlying $PbSO_4$ membrane is optically transparent and α-PbO is the only photoactive lead phase to produce an appreciable photocurrent in the visible region of the spectrum.

Traditional measurements obtained by photocurrent spectroscopy are macroscopic in the sense that the whole electrode surface is perturbed by the light stimulus. Consequently, the photocurrent response induced by the stimulus appears as an average response and any localized information is lost. When a focused laser source is used, it provides a localized probe and, therefore, direct information on the distribution of a photoactive phase can be obtained, at least on the microscopic scale. Photocurrent imaging techniques based on this principle have been developed in recent years for examination of electrochemical interfaces [31–38].

In this paper, a scanning laser imaging technique is used to map, *in situ*, the spatial distribution of α-PbO in corrosion films of the type formed on lead/acid battery grids. In view of the foregoing discussion, Pb–Ca and Pb–Sb grids taken from cycled batteries have been examined. Results are also presented from a study of the corrosion film produced on Pb–Ca and tin-coated Pb–Ca grids in the absence of active material. An *ex situ* technique for revealing the distribution of the α-PbO across corrosion film/grid transverse sections is described and applied to a sample of Pb–Ca grid.

Experimental

The scanning laser microscope is shown schematically in Fig. 1. A focused laser spot (He/Cd, 442 nm) is rastered (through the use of mirrors) over the surface of the sample by scanning the light beam. Localized photocurrent measurements for each individual beam position are accumulated in a frame store and then retrieved in the form of a grey-scale image. The TV frame store system (576 lines $\times$ 530 pixels, 8-bit accuracy) also generates the control signals to drive the mirrors. Each particular memory location in store is therefore associated with a particular physical position of the beam on the surface of the sample. Magnification is controlled by the amplitude of the scanning signals that are applied to the mirrors (i.e., the deflection of the mirrors) and the frequency of these signals limits the data acquisition rate to the range: 5 ms to 200 s per line. At these speeds, mirror scanning allows a study of the time evolution of the surface (for example, during anodic growth) at a maximum rate of an image every 2 s. A beam splitter, positioned on the optical path immediately in front of the mirrors, collects the light reflected off the electrode surface into a sensitive silicon photodiode. This provides an optical image of the surface that is exactly coincident with the photocurrent image.

The electrochemical instrumentation controls the potential across the sample/electrolyte interface. The photocurrent output is d.c.-coupled through an amplifier stage and offset to match the incoming signal to the input range of the image processor. The image contrast therefore represents variations in photocurrent across the surface.

There are two general methods to process the photoresponse, as shown in Fig. 2. In one technique, the beam is intensity modulated using an optical chopper or a photoacoustic modulator, and then the signal is processed with a lock-in amplifier. This mode 'continuous scan, lock-in detection' is relatively slow; the frame-acquisition rates usually exceed 20 min. Nevertheless, this procedure is necessary when the signals

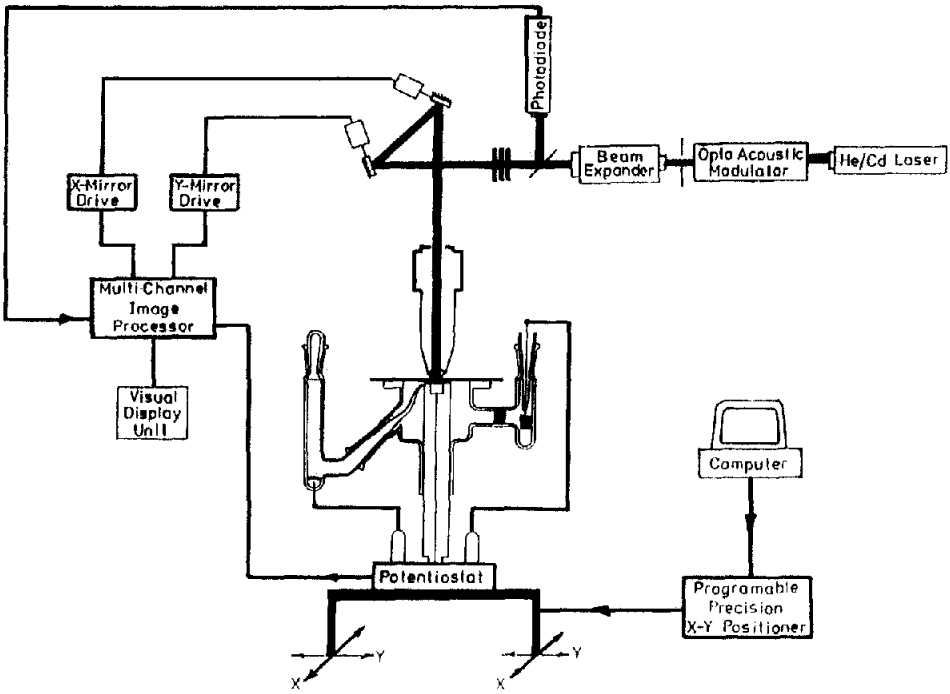

Fig. 1. Schematic diagram of the instrumentation for scanning laser photoelectrochemical microscopy.

are weak or the background dark-current is noisy. An alternative approach is 'continuous-scan, direct detection'. Here, the beam intensity is kept constant and the variations in the signal are imaged directly. This latter method often requires the time-independent part of the response (dark current) to be offset to match the incoming signal to the input range of the image processor. The contrast obtained with these two general imaging methods produces different information. The lock-in detection mode is an averaged response over the time-scale of the modulation frequency, whereas the direct detection method contains transient information that appears as streaking across the image along the direction of the line scan. These transient features provide extra information on the kinetics of either the electrochemical reactions or the recombination processes.

The mode of operation of the mirrors follows a sequence in which the image is created by moving the beam from left to right, and top to bottom, across a region of the sample. This is also the orientation of the images as presented below in the Figs. 4 to 12. Unless stated specifically in the figure caption, the direct detection method has been used. Image processing is also available to improve the signal/noise ratio by accumulating data over a number of frames (integration). The differential amplifier was operated in d.c.-coupled mode and filtration of the signal was kept to a minimum.

Samples of positive plate were vacuum impregnated with epoxy resin and cut into blocks (Fig. 3); full details of the processing and service history of these samples are given in ref. 39. Individual samples were cut and polished to reveal a cross section

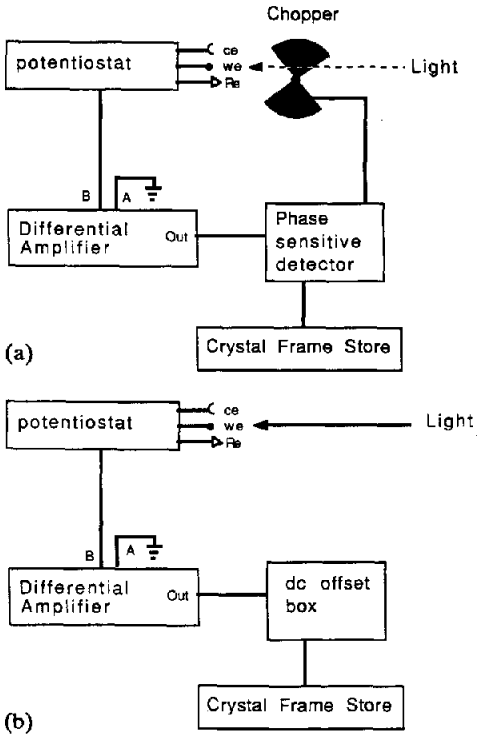

Fig. 2. Schematic diagram of the signal-processing instrumentation for: (a) continuous scan, lock-in detection; (b) continuous scan direct detection imaging mode.

through the alloy and the accompanying corrosion layer. The reverse face was used as the working-electrode contact. In addition, some Pb–Ca grids, with or without tin coating, were subjected to corrosion tests. Specimens taken from these grids were cast in epoxy resin and polished to reveal a cross section through the alloy and accompanying corrosion layer. Before each experiment, the sample was subjected to a light polish on 0.05 μm alumina to remove the tarnish, and then examined using a Hitachi 5200 scanning electron microscope (SEM). Image degradation due to charging effects was tolerated in order to avoid coating the sample with gold. Potentials were measured with respect to a $Hg/Hg_2SO_4/1$ M H_2SO_4 reference electrode. The solution in all cases was 1 M H_2SO_4.

For the *ex situ* characterization technique, a contact was made to the paste with silver paint and the position-sensitive photovoltage signal between this contact and the lead-alloy grid was measured. This technique was first proposed by Shea and Michels [40]. Later, Bullock and Butler [19] demonstrated the presence of a photoactive phase across the corrosion layer/alloy boundary by using a single-line scan technique.

Results

The SEM image given in Fig. 4(a) shows the basic structure of a sample that consists of a fresh exposed triangular surface of the alloy metal, a corrosion layer, and part of the formed active material. This sample is a transverse section through

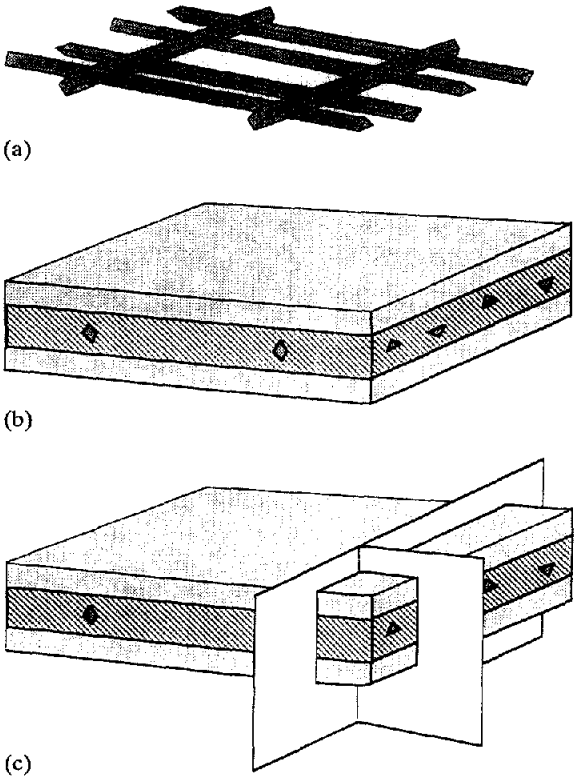

Fig. 3. Configuration of samples of positive plate: (a) structure of the alloy grid; (b) a 'block' of plate, the middle layer is epoxy-impregnated active material, the outer layers are epoxy resin; (c) method of sectioning to prepare samples.

a plate with a Pb–0.09wt.%Ca grid and was removed immediately after plate formation. In this paper, it is necessary to distinguish between photoactivity within the inherent corrosion layer that is concentric to the grid, and within the corrosion film that forms on the surface exposed during preparation of the cross section. The latter product – henceforth, referred to as the corrosion 'film' – will be formed immediately after the sample is placed in the electrochemical cell and will grow under the action of an applied potential (Fig. 1). The sample was immersed in acid and held at a potential of -0.2 V. An optical image was obtained with an attenuated beam intensity of power 2 μW. This procedure allowed the laser beam to be focused on the electrode surface, and the low intensity ensured that the light behaved only as a passive probe of the system properties.

At the applied potential, the surface was covered with a membrane of $PbSO_4$ but this did not degrade significantly the optical image. The potential was stepped to 0 V and the beam intensity was increased (power 2 mW) to obtain the photocurrent images shown in Figs. 4(b) to (d). This potential regime was chosen specifically to avoid nucleation and growth of α-PbO on the fresh, exposed grid surface. A photoactive region associated with the corrosion layer that was produced during the formation process can be seen clearly around the circumference of the alloy, Fig. 4(b). At higher

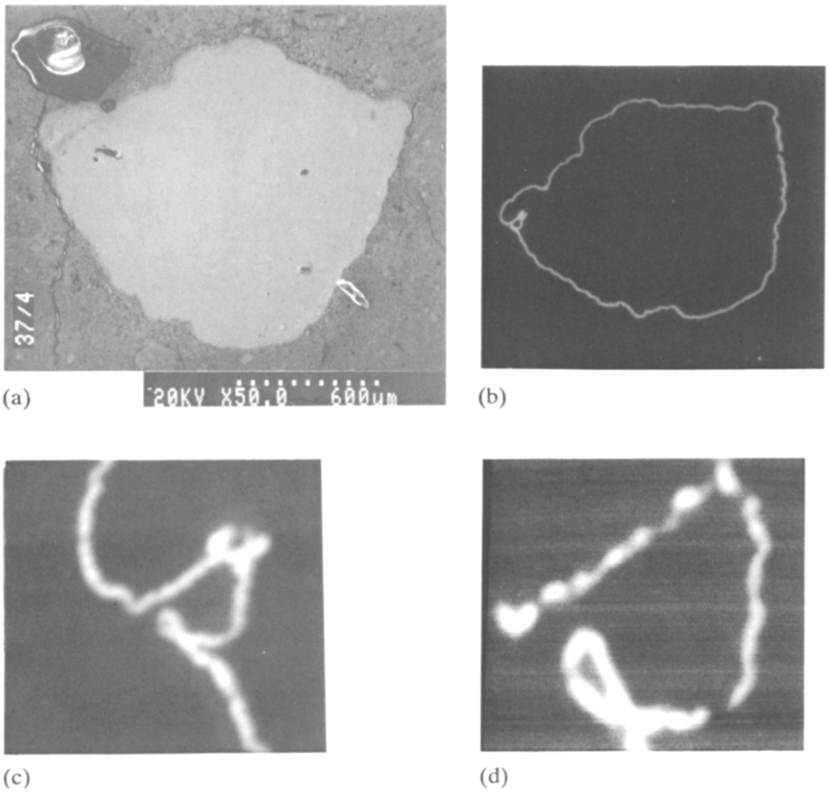

Fig. 4. Characterization of a Pb–Ca grid transverse section after formation: (a) SEM micrograph; (b) photocurrent image in 1 M H_2SO_4; (c) and (d) photocurrent image of the corrosion layer corresponding to region centre left of (b) after increasing the magnification. Conditions are as follows: (b) E = 0 V, line scan rate 7.2 ms/line, contrast range is 0 (black) to 500 nA (white), λ = 442 nm, power = 1.98 mW; (c) E = 0 V, line scan rate 30 ms/line, contrast range is 0 (black) to 500 nA (white), λ = 442 nm, power = 198 μW; (d) E = 0 V, line scan rate 7.2 ms/line, contrast range is 0 (black) to 200 nA (white), λ = 422 nm, power = 198 μW.

magnification, Fig. 4(c), it appears that this layer consists of interconnecting lenses of higher photoactivity. It is also observed that the layer is slowly losing photoactivity in parts to reveal a more defined, lenticular structure Fig. 4(d). The photoactive band is of the order of 5 μm in thickness. At the higher magnification, contrast is apparent on the background surface and is aligned with the direction of the scan (horizontal streaks, left to right across image). This feature could be due to fluctuations in the dark-current signal that are modified by the time response of the differential amplifier.

The effect of increasing the anodic potential of the alloy is shown in the photocurrent images of Figs. 5 and 6. After 2 h at 0 V, a photoactive film had not been formed on the freshly exposed alloy surface although the response within the corrosion layer (Fig. 5(a)) had changed as indicated in Fig. 4, above. No difference in behaviour was observed on stepping the potential to +0.1 V (10 min), +0.2 V (10 min), and 0.3 V (30 min). At +0.4 V, there was a rapid visible change as localized film growth took place on the alloy surface, Fig. 5(b). This was accompanied by noise fluctuations in the dark current, as seen in the streaked background contrast.

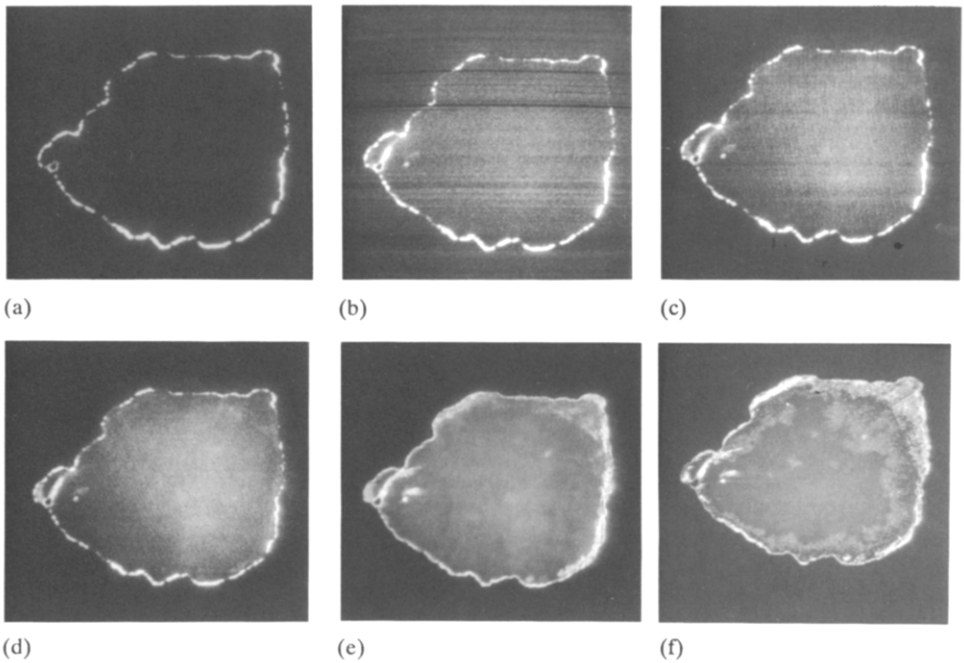

Fig. 5. Photocurrent images of a Pb–Ca grid transverse section in 1 M H_2SO_4 at: (a) E = 0 V; (b) E = +0.4 V; (c) E = +0.5 V; (d) E = +0.6 V; (e) E = +0.7 V; (f) E = +0.9 V. Conditions are as follows: (a)–(e) line scan rate 30 ms/line, contrast range is 0 (black) to 500 nA (white), λ = 442 nm, power = 1.98 mW; (d) is an integrated image over 8 frames; (f) line scan rate 30 ms/line, contrast range is 0 (black) to 500 nA (white), λ = 442 nm, power = 198 μW, integrated 16 frames.

At +0.5 to +0.9 V (Figs. 5(c) to (f)), the film growth appeared to proceed by the successive nucleation of concentric patches that moved inwards, i.e., towards the centre of the grid. The continuity of the corrosion layer had virtually reformed (cf., Fig. 5(a)) and the dark current was stable. A change in this pattern was revealed by stepping the potential to +1.0 V, Fig. 6(a). A patch appeared towards the centre of the alloy and followed the trend previously observed for increasing potential. It was noted, however, that part of the film produced during the potential step to 0.9 V had lost its photoactivity. This implied a lower overpotential for oxidation of the α-PbO on that part of the surface. At higher potentials of +1.1 and +1.2 V (Figs. 6(b), (c)), photoactivity was maintained and the dark current once again became noisy due to oxidation of the film and possible formation of gas bubbles. Finally, on stepping back to +0.8 V (Fig. 6(d)), it was noted that photoactivity actually decreased in the centre of the alloy surface, but was maintained at the edges of the alloy and also in the corrosion layer. These results clearly demonstrate that the Pb–Ca alloy surface is heterogeneous with respect to the overpotential required for the formation of the photoactive phase and its subsequent oxidation to PbO_2. The observations also indicate that α-PbO can exist in the potential environment that corresponds to the 'top-of-charge' in positive battery plates. In all of these images, there is no indication of penetration of a photoactive phase into the active material that surrounded the grid.

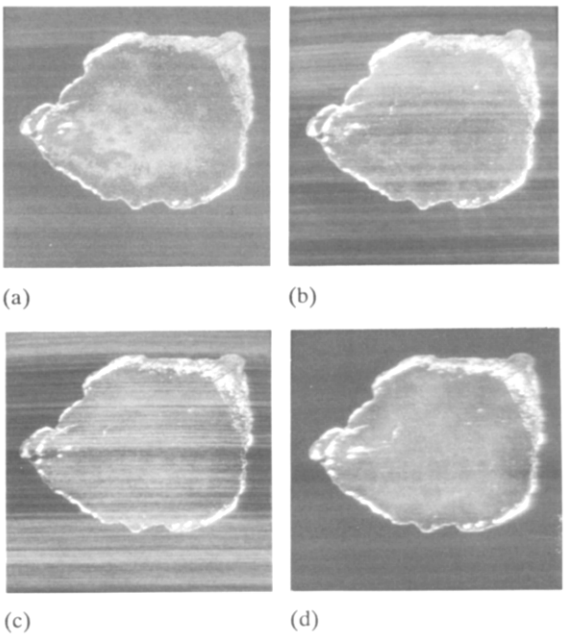

Fig. 6. Photocurrent images of a Pb–Ca grid transverse section in 1 M H_2SO_4 at: (a) E = 1.0 V; (b) E = +1.1 V; (c) E = +1.2 V; (d) E = +0.8 V. Conditions are as follows: (a) line scan rate 30 ms/line, constant range is 0 (black) to 500 nA (white), λ = 442 nm, power = 1.98 mW, integrate 8 frames; (b) line scan rate 30 ms/line, contrast range is 0 (black) to 2 μA (white), λ = 442 nm, power = 1.98 mW, integrated 8 frames; (c) line scan rate 30 ms/line, contrast range is 0 (black) to 2 μA (white); λ = 442 nm; power = 1.98 mW, a.c.-coupled input; (d) line scan rate 30 ms/line, contrast range is 0 (black) to 200 nA (white), λ = 442 nm, power = 198 mW, integrated 8 frames.

A similar set of results was obtained on an equivalent plate sample with a Pb–5.7 wt.%Sb–0.3wt.%Sn grid. This alloy is hereafter designated 'Pb–Sb'. The data are shown in Figs. 7 and 8. The routine for examination followed the procedures outlined for the Pb–Ca sample, but the sampled grid section was of a different shape. The optical image and the corresponding photocurrent image are shown in Figs. 7(a) and (b), respectively. Two points are to be noted. First, it is curious that a photocurrent is observed on the active material and also on the bare alloy. Second, the corrosion layer is visible on the image but the response is feeble in comparison with that observed on the Pb–Ca sample after plate formation, Fig. 4(b).

The effect of potential on the photocurrent image was observed on a different area of the same sample, Fig. 7(c). The photocurrent contrast on the bare alloy remained unchanged until the potential of the sample reached +0.3 V. The signal associated with the corrosion layer partially disappeared with time to leave small lenses of photoactive material. These features are shown in Fig. 7(d). At a potential of +0.6 V, the structure of the film changed (Figs. 7(e), (f)); it became more dendritic in appearance. After 3 h at that potential (Fig. 8(a)), the corrosion film appeared as a tangled mass of dendritic structures, and the photocurrent signal was an order of magnitude greater than that observed on the Pb–Ca sample. The roughness of the bare alloy surface was visible and there were holes within the film that were not photoactive. The contrast of the holes fluctuated on the tens-of-minutes timescale.

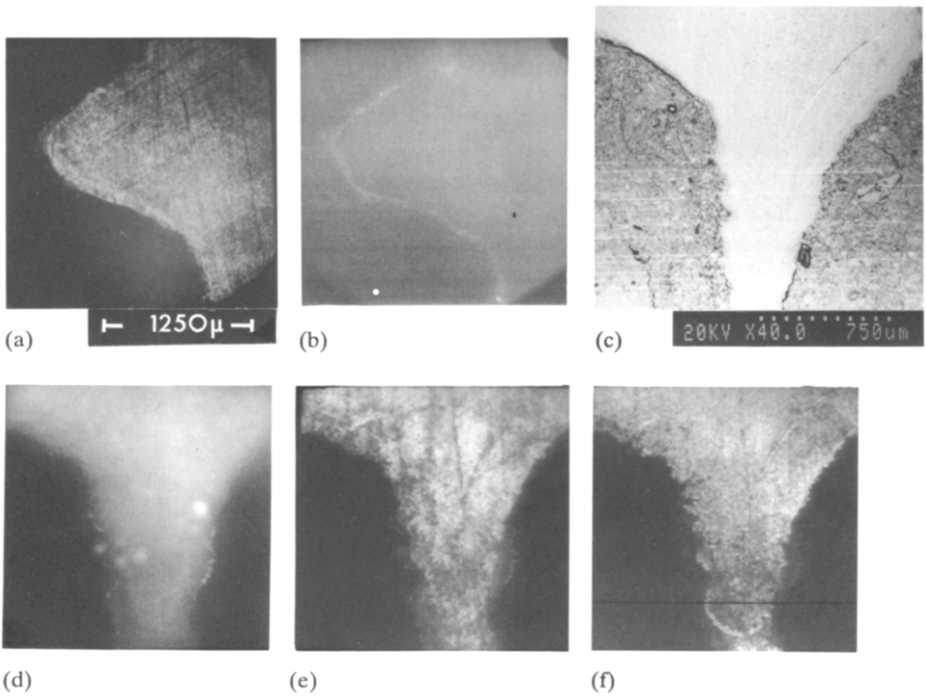

Fig. 7. Photocurrent images of a Pb–Sb grid transverse section in 1 M H_2SO_4: (a) *in situ* optical image; (b) photocurrent image at +0.3 V; (c) SEM image of the section; (d)–(f) photocurrent images at +0.3, +0.6 and +0.6 V, respectively. Conditions are as follows: (b) line scan rate 30 ms/line, contrast range is 0 (black) to 1 μA (white), $\lambda = 442$ nm, power = 1.98 mW, integrated 16 frames; (d) line scan rate 30 ms/line, contrast range is 0 (black) to 1 μA (white), $\lambda = 442$ nm, power = 1.98 mW, integrated 32 frames; (e) after potential step to +0.6 V, line scan rate 30 ms/line, contrast range is 0 (black) to 5 μA (white), $\lambda = 442$ nm, power = 1.98 mW, integrated 16 frames; (f) after 30 min at +0.6 V, line scan rate 30 ms/line, contrast range is 0 (black) to 5 μA (white), $\lambda = 442$ nm, power = 1.98 mW, integrated 16 frames.

This suggests that a slow formation/dissolution process is occurring within the corrosion film. Photocurrent images at +0.8 and +0.9 V (Figs. 8(b), (c)) show clearly the formation of dendritic structures. These are particularly well-defined along the right-hand alloy/active-material boundary. The effects of reducing this corrosion film at a potential of +0.6 V are shown in Fig. 8(d). Noteworthy is the black streak contrast at intervals along the right-hand alloy/active-material boundary. The dark-current signal has been offset in this image to the grey value as seen on the active material. Thus, the white regions represent anodic photocurrent and the black streaks represent cathodic photocurrent transients with a time constant of the order of a few ms. Further reduction at +0.2 V indicates a slow breakdown of the dendritic structure, Figs. 8(e), (f). Transient features in the photocurrent persist, but are now only associated with the material in the corrosion layer and are visible at both alloy/active-material boundaries.

A preliminary comparison was made of the corrosion layers on tin-coated and untreated Pb–Ca grids that had undergone extensive attack. The electron micrograph and the corresponding photocurrent image are shown in Figs. 9 and 10 for the tin-coated and bare alloys, respectively. The analysis routine was the same as that used for the previous samples, i.e., an optical image was obtained at low laser intensity

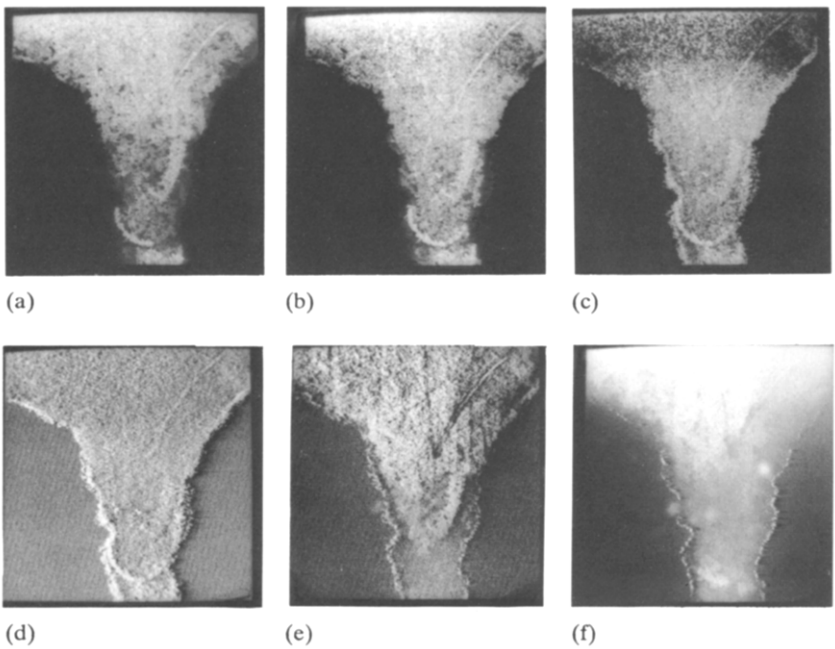

Fig. 8. Photocurrent images of a Pb–Sb grid transverse section in 1 M H_2SO_4 at: (a) E = +0.6 V; (b) E = +0.8 V; (c) E = +0.9 V; (d) E = +0.6 V; (e) E = +0.2 V; (f) E = +0.2 V. Conditions are as follows: (a) after 3 h at +0.6 V, line scan rate 30 ms/line, contrast range is 0 (black) to 5 μA (white), λ = 442 nm, power = 1.98 mW, integrated 16 frames; (b), (c) line scan rate 30 ms/line, contrast range is 0 (black) to 5 μA (white), λ = 442 nm, power = 1.98 mW, integrated 16 frames; (d) line scan rate 30 ms/line, contrast range is −2 μA (black) to 3 μA (white), λ = 442 nm, power = 1.98 mW; (e) line scan rate 30 ms/line, contrast range is −200 nA (black) to 800 nA (white), λ = 442 nm, power = 1.98 μW; (f) after 2 h at +0.2 V, line scan rate 30 ms/line, contrast range is −200 nA (black) to 800 nA (white), λ = 442 nm, power = 1.98 mW.

followed by the photocurrent image at 0 V. Photocurrent signals were particularly weak and images could only be acquired in the continuous scan, lock-in detection mode. Examination of the data in Fig. 9 reveals that there is no evidence of a continuous photoactive layer around the circumference of the tin-coated sample (as, for example, in Fig. 4(b)). There are, however, some variations in contrast within the corrosion layer and these indicate the development of isolated, small patches of α-PbO. There are also (black) regions that are not photoactive; comparison with the electron micrographic image suggests that these regions correspond to the localized formation of massive $PbSO_4$ crystals. The tin-free Pb–Ca grid (Fig. 10) shows a discontinuous photoactive layer around the perimeters of the alloy and a large enclosed cavity. In these regions, the photocurrent is four times larger than that given by the tin-coated sample. These results support the observation that a tin coating increases the performance of Pb–Ca grids by suppressing the formation of α-PbO.

An alternative approach for the analysis of transverse sections is to construct a solid-state photocell of the design as shown in Fig. 11. Results of photovoltage variations across such a configuration (in this case, a silver/active material/corrosion layer/lead photocell) are presented in Fig. 12 for a section of Pb–Ca plate that had completed 51 cycles. In the optical image (Fig. 12(a)), the active material is shown on the left

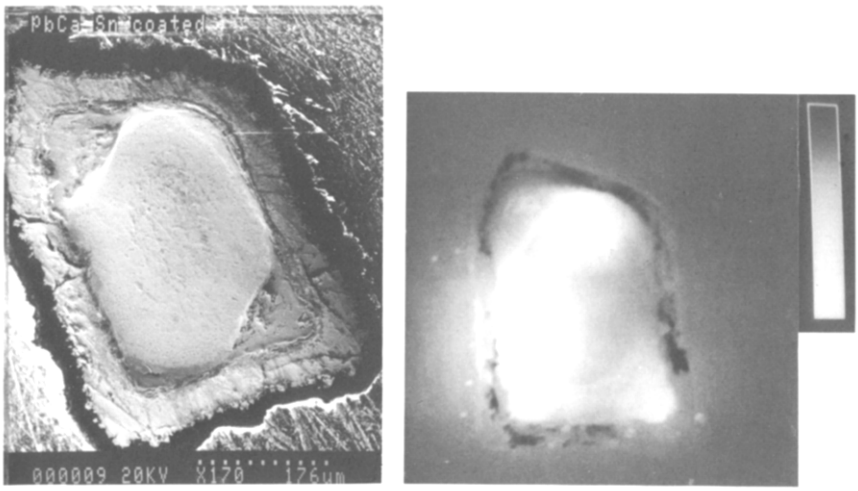

(a) (b)

Fig. 9. Characterization of a tin-coated Pb–Ca grid transverse section after cycling: (a) SEM micrograph; (b) photocurrent image in 1 M H_2SO_4 at E = 0 V. Conditions are as follows: (b) continuous-scan, lock-in detection mode, modulation frequency 2.86 kHz, line scan rate 1.99 s/line, contrast range is 0 (black) to 1 nA (white), $\lambda = 442$ nm, power = 1.98 mW, PSD time-constant 3 ms.

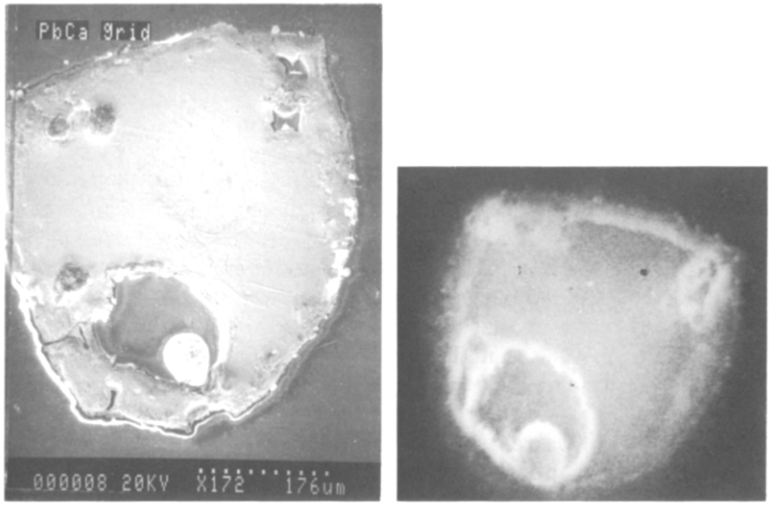

(a) (b)

Fig. 10. Characterization of a Pb–Ca grid transverse section after cycling: (a) SEM micrograph; (b) photocurrent image in 1 M H_2SO_4 at E = 0 V. Conditions are as follows: (b) continuous-scan, lock-in detection mode, modulation frequency 2.86 kHz, line scan rate 3 s/line, contrast range is 0 (black) to 20 nA (white), $\lambda = 442$ nm, power = 1.98 mW, PSD time-constant 3 ms.

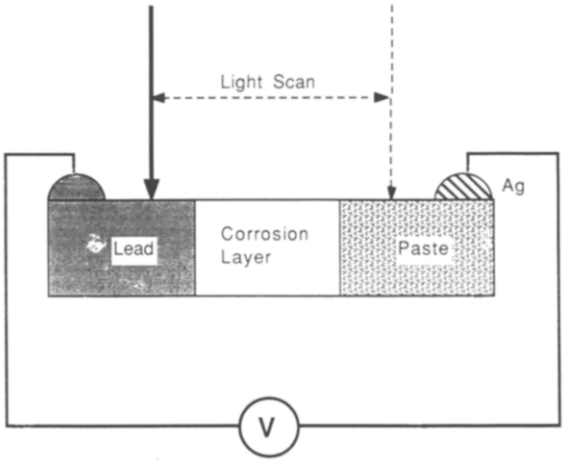

Fig. 11. Schematic diagram of solid-state photocell.

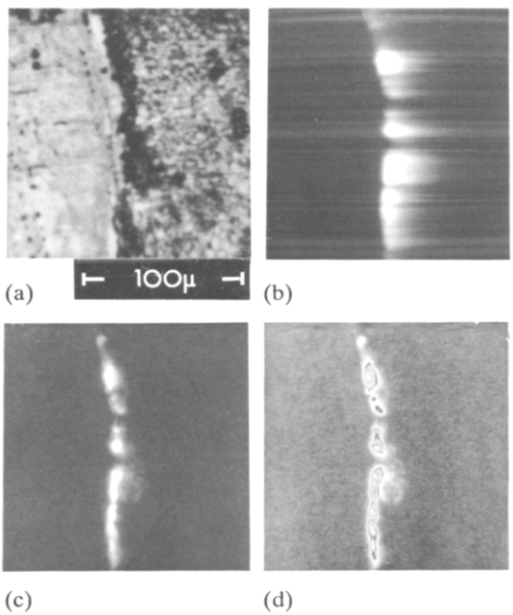

Fig. 12. Characterization of a Pb–Ca grid transverse section after cycling: (a) SEM micrograph; (b)–(d) photovoltage images of a silver/active material/corrosion layer/lead-alloy photocell. Conditions are as follows: (b) line scan rate 30 ms/line, contrast range is 0 (black) to 100 μV (white), $\lambda = 442$ nm, power = 1.98 mW; (c) continuous-scan, lock-in detection mode, modulation frequency = 2.86 kHz, line scan rate 1.99 s/line, contrast range is 0 (black) to 10 μV (white), $\lambda = 442$ nm, power = 1.98 mW, PSD time-constant 3 ms; (d) as (c) but with a stretched contrast scale as shown.

and the grid is on the right. The dark central band is the corrosion layer. At this magnification, the resolution is degraded by slight movement due to vibration. The photovoltage image, Fig. 12(b), was obtained by a fast-scan velocity and shows that

the edge between the active material and the corrosion layer is sharply defined. The corrosion-layer/alloy boundary is smeared by the transient effect that arises from what can be effectively viewed as a pulse of illumination that moves across the surface. The structure on the alloy side of the boundary is resolved using the continuous scan, lock-in detection mode, and is shown in Fig. 12(c). The distribution of the photoactive phase is discontinuous. The fine structure of the layer is revealed by using the expanded contrast scale, Fig. 12(d).

In the case of the cycled Pb–Ca grid (Fig. 12(c)), the alloy in the central region of the image is preferentially corroded. Within the vicinity of the penetrating corrosion, there is a hint of a photoactive phase next to the alloy but the main photoactivity follows the active-material/corrosion-layer boundary. If it is assumed that this marks the position of the original corrosion-layer/alloy boundary during plate formation, it then follows that the α-PbO developed during this process is maintained, at least in part, throughout the life of the plate.

Discussion

The photocurrent spectroscopy of the corrosion layers on lead and its alloys has been the subject of detailed study and discussion. The older literature favours a model based on the formation of a nonstoichiometric compound PbO_x [41, 42]. According to this model, α-PbO does not display photoelectrochemical properties until it is photoactivated. This is a process during which the photoconductivity of the α-PbO layer increases as a consequence of illumination. The mechanism of photoactivation involves the formation of high-energy oxygen species as a product of the oxidation of adsorbed hydroxyl ions (at the PbO/membrane interface) by the photogenerated holes. The electric field draws these product species into the lattice and thus PbO_x is formed.

Recently, Peter and co-workers [26–28, 43] have contested the existence of PbO_x. They have shown that photocurrents can be observed at low-illumination levels without photoactivation, and that the photoactive phase formed by the oxidation of lead, as well as by the reduction of PbO_2, is in fact α-PbO. This evidence is based on a comparison of the photocurrent spectra observed in acid and alkaline solutions with the published absorption spectra for α-PbO. It is known that α-PbO behaves as a quasi-intrinsic semiconductor as a result of its microcrystallinity [44]. The cathodic reduction of a film of α-PbO_2 is incomplete and consists of a mixture of α-PbO and α-PbO_2. It is argued that the α-PbO_2 acts as a current-collecting matrix that connects the microcrystallites of α-PbO. Passivation occurs when there is insufficient α-PbO_2 left to maintain conducting pathways through the insulating α-PbO. At high intensities, the process of photoactivation can be viewed as a photo-oxidation that leads to an increase in the PbO_2/PbO ratio. The interconnectivity of the degenerate PbO_2 matrix now serves to increase the fraction of photogenerated carriers that are registered in the external measuring circuit.

The question as to whether the focused beam in the scanned experiment behaves as a passive probe or induces photoactivation is difficult to assess. The power of the beam at 2 mW is low compared with the 100 W tungsten source that is used for photoactivation, but for a focused beam with diameter of the order of 5 μm the power density is substantial. During a scanned experiment, however, this high power density is only applied to a particular spot on the surface for a fraction of the total frame acquisition time. At a scan rate of 30 ms/line, for example, an individual spot is illuminated for 60 μs and this is followed by a 16 s dark period. For Pb–Ca and

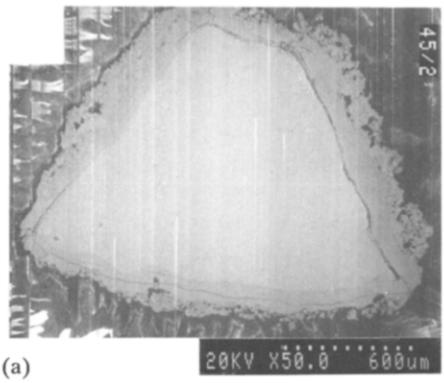

(a)

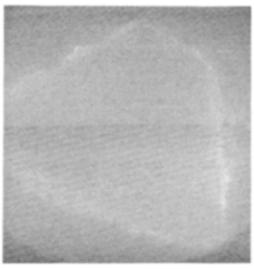

(b)

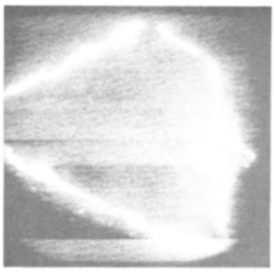

(c)

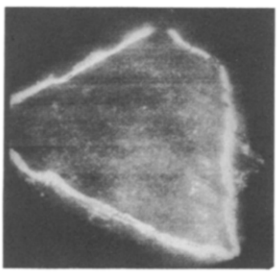

(d)

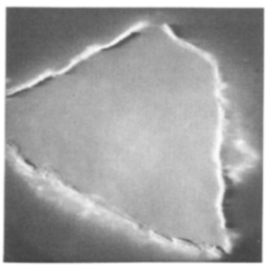

(e)

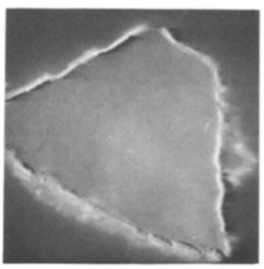

(f)

Fig. 13. Characterization of a Pb–Sb grid transverse section after cycling: (a) SEM image; (b)–(f) photocurrent images in 1 M H_2SO_4 at E = +0.6 V. (b)–(d) represent the 1st, 7th and 13th image, respectively. Conditions are as follows: (b), (c) line scan rate 199 ms/line, contrast range is 0 (black) to 1 μA (white), λ = 442 nm, power = 1.98 mW; (d) line scan rate 199 ms/line, contrast range is 0 (black) to 2 μA (white), λ = 442 nm, power = 1.98 mW; (e), (f) following a triangular potential ramp from +0.6 to 1.2 and 1.35 V, respectively, in the dark at 10 mV/s, line scan rate 30 ms/line, contrast range is 0 (black) to 2 μA (white), λ = 442 nm, power = 1.98 mW.

Pb–Sb grids from formed plates (Figs. 4 and 7), as well as for the *ex situ* sample (Fig. 12), there was no evidence of photoactivation. A Pb–Sb sample taken from a cycled plate and polarized at +0.6 V exhibited increased photoactivity with each successive frame. This is shown in the images of Figs. 13(b), (c) and (d) that were collected during the 1st, 7th and 13th frames respectively. This result is not, however,

conclusive proof of photoactivation as the increased photocurrent could arise at this potential from a thickening of the α-PbO phase within the corrosion layer over the long timescale of the experiment. Some growth of a corrosion film on the exposed alloy surface (Fig. 13(d)) confirms this possibility.

It is interesting to note that if the potential is ramped into the lead dioxide region in the dark and then the photocurrent image is again recorded at +0.6 V, there is an increase in the resolution of the corrosion layer. This is shown in Figs. 13(e) and (f) following linear sweep voltammetry to +1.2 and +1.35 V, respectively. Transients are also observed in these images, and show that subtle changes in the structure of the corrosion layer have occurred. The reverse voltammogram indicates that there has been some oxidation of the layer to PbO_2.

Conclusions

It has been demonstrated that the technique of photocurrent imaging has sufficient resolution to characterize the distribution of photoactive phases within the corrosion layers formed on battery grids during plate formation and charge/discharge cycling.

Preliminary observations have shown that a substantial layer of α-PbO is present on a Pb–Ca grid after formation compared with a similar grid made of Pb–Sb. The surface of the bare alloy is heterogeneous with respect to the nucleation and growth of α-PbO and its subsequent oxidation to PbO_2. The morphology of the resulting corrosion film is different on the Pb–Sb and Pb–Ca alloys. On Pb–Sb, the structure is both dendritic and thicker than on Pb–Ca. The latter results are surprising and are contrary to observations published by other workers. In addition, it is further claimed [27] that the film on a Pb–4wt.%Sb alloy is thinner than the corresponding film on pure lead. It would appear that the factor of two increase in photocurrent on the Pb–Sb sample is due to an increase in the thickness of material that is available to absorb the light. An alternative is that recombination processes are suppressed and/or carrier capture to the electrolyte phase is increased by the presence of antimony.

Acknowledgements

The authors gratefully acknowledge support from the International Lead Zinc Research Organization. Thanks are also due to L. T. Lam (CSIRO Division of Mineral Products) for assistance with the preparation of plate and grid materials.

References

1 S. Tudor, A. Weisstuch and S. V. Davang, *Electrochem. Technol., 3* (1965) 90; *4* (1966) 406; *5* (1967) 21.

2 S. Hattori, M. Yamaura, M. Kono, M. Yamane, H. Nakashima and J. Yamashita, *ILZRO Project LE-253 Rep. for Period Mar.–Nov., 1977,* International Lead Zinc Research Organization, Inc., Research Triangle Park, NC, USA, Dec. 15, 1977.

3 H. Tamura, H. Yoneyama, C. Iwakura and O. Ikeda, *ILZRO Project LE-254, Final Rep.,* International Lead Zinc Research Organization, Inc., Research Triangle Park, NC, USA, Dec. 31, 1977.

4 H. Nakashima and S. Hattori, *Proc. Pb80, 7th Int. Lead Conf., Madrid, Spain, May 12–15, 1980,* p. 88.

5 K. Fuchida, K. Okada, S. Hattori, M. Kono, M. Yamane, T. Takayama, J. Yamashita and Y. Nakayama, *ILZRO Project LE-276, Final Rep. (Prog. Rep. No. 8)*, International Lead Zinc Research Organization, Inc., Research Triangle Park, NC, USA, Mar. 31, 1982.
6 A. Komaki, G. Kawamura and S. Mochizuki, *Prog. Batteries Solar Cells, 4* (1982) 167.
7 T. G. Chang and E. M. L. Valeriote, *J. Electrochem. Soc., 132* (1985) 1783.
8 B. J. Carter, S. Di Stefano and L. Whitcanack, *Ext. Abstr.*, Proc. Vol. 86-2, The Electrochemical Society, Pennington, NJ, 1986, Abstr. no. 94, p. 133.
9 A. Kita, Y. Matsumaru, M. Shinpo and H. Nakashima, in L. J. Pearce (ed.), *Power Sources 11: Research and Development in Non-Mechanical Electrical Power Sources*, International Power Sources Symposium Committee, Leatherhead, UK, 1987, p. 31.
10 M. Tsubota, S. Osumi and M. Kosai, *J. Power Sources, 33* (1991) 105.
11 E. M. L. Valeriote, A. Heim and M. S. Ho, *J. Power Sources, 33* (1991) 187.
12 A. F. Hollenkamp, *J. Power Sources, 36* (1991) 567.
13 A. Winsel, E. Voss and U. Hullmeine, *J. Power Sources, 30* (1990) 209.
14 H. K. Geiss, in K. R. Bullock and D. Pavlov (eds.), *Proc. Symp. Advances in Lead/Acid Batteries*, Proc. Vol. 84-14, The Electrochemical Society, Pennington, NJ, 1984, pp. 241–251.
15 R. F. Nelson and D. M. Wisdom, *J. Power Sources, 33* (1991) 165.
16 D. Pavlov, C. N. Poulieff, E. Klaja and N. Iordanov, *J. Electrochem. Soc., 116* (1969) 316.
17 D. Pavlov and N. Iordanov, *J. Electrochem. Soc., 117* (1970) 1103.
18 P. Ruetschi, *J. Electrochem. Soc., 120* (1973) 331.
19 K. R. Bullock and M. A. Butler, *J. Electrochem. Soc., 133* (1986) 1085.
20 W. Mindt, *J. Electrochem. Soc., 116* (1969) 1076.
21 S. Fletcher and D. B. Matthews, *J. Electroanal. Chem., 126* (1981) 131.
22 A. M. Hardman, R. T. Hopwood, J. E. Manders, D. A. J. Rand, J. W. Reitz and H. Tuphorn, *J. Power Sources, 23* (1988) 257.
23 R. J. Hill, *J. Solid State Chem., 71* (1987) 12.
24 D. E. Swets, *J. Electrochem. Soc., 120* (1973) 925.
25 B. Culpin, A. F. Hollenkamp and D. A. J. Rand, *J. Power Sources, 38* (1992) 63.
26 J. S. Buchanan, N. P. Freestone and L. M. Peter, *J. Electroanal. Chem., 182* (1985) 383.
27 J. S. Buchanan and L. M. Peter, *Electrochim. Acta, 33* (1988) 127.
28 S. A. Campbell and L. M. Peter, *Electroanal. Chem., 309* (1991) 213.
29 L. M. Peter, *Surf. Sci., 101* (1980) 162.
30 G. H. Brilmyer, in K. R. Bullock and D. Pavlov (eds.), *Proc. Symp. Advances in Lead/Acid Batteries*, Proc. Vol. 84-14, The Electrochemical Society, Pennington, NJ, 1984, pp. 142–153.
31 M. A. Butler, *J. Electrochem. Soc., 130* (1983) 2185.
32 M. A. Butler, *J. Electrochem. Soc., 131* (1984) 2385.
33 R. Peat, A. J. Kucernak, D. E. Williams and L. M. Peter, *Semicond. Sci. Technol., 5* (1990) 914.
34 R. Peat, A. R. Kucernak and D. E. Williams, *Electrochim. Acta, 37* (1992) 933.
35 A. R. J. Kucernak, R. Peat and D. E. Williams, *Electrochim. Acta, 38* (1993) 57.
36 A. R. J. Kucernak, R. Peat and D. E. Williams, *J. Electrochem. Soc., 139* (1992) 2337.
37 R. Peat, P. T. Moseley, T. L. Lam and D. A. J. Rand, *J. Power Sources, 38* (1992) 373.
38 A. Kucernak, R. Peat and D. E. Williams, *J. Electrochem. Soc., 138* (1991) 1645.
39 A. F. Hollenkamp, M. J. Koop, A.-M. Huey, K. K. Constanti, J. A. Hamilton, L. Apateanu and L. H. Vu, *ILZRO Project LE-371, Prog. Rep. 4: Jan.–July 1992*, International Lead Zinc Organization, Inc., Research Triangle Park, NC, USA, Aug. 1992.
40 M. J. Shea and W. C. Michels, *J. Chem. Phys., 59* (1972) 2764.
41 D. Pavlov, *J. Electroanal. Chem., 118* (1981) 167–185.
42 D. Pavlov, S. Zanova and G. Papazov, *J. Electrochem. Soc., 124* (1977) 1522.
43 L. M. Peter, *J. Electroanal. Chem., 144* (1983) 315.
44 J. van den Broek, *Philips Rep., 22* (1967) 367.